Effect of bonding and static atomic displacements on composition quantification in $In_xGa_{1-x}N_yAs_{1-y}$

Knut Müller,* Marco Schowalter, and Andreas Rosenauer
Universität Bremen, Otto-Hahn-Allee 1, 28359 Bremen, Germany

Oleg Rubel
Thunder Bay Regional Research Institute, 290 Munro Street, Thunder Bay, Canada ON P7A 7T1;
Lakehead University, 955 Oliver Road, Thunder Bay, Canada ON P7B 5E1;
and Philipps Universität Marburg, Hans-Meerwein-Straße, 35032 Marburg, Germany

Kerstin Volz
Philipps Universität Marburg, Hans-Meerwein-Straße, 35032 Marburg, Germany

(Received 5 November 2009; revised manuscript received 26 January 2010; published 19 February 2010)

This study addresses the influence of static atomic displacements (SAD) and chemical bonding in (InGa)(NAs) alloys on structure factors for electron scattering and stresses their importance for compositional analysis. First, SAD are derived using valence force field (VFF) methods and their reliability is demonstrated by calculating residual atomic forces using density-functional theory (DFT). A systematic study of structure factors for low indium and nitrogen contents is given by means of full DFT calculations on the one hand and atomistic models on the other. We show that the consideration of SAD via VFF together with the inclusion of bonding via modified atomic scattering amplitudes is in best agreement with a full DFT calculation, providing the possibility to include bonding effects also if large cells containing 10^6 atoms are considered. Second, a technique is presented, which allows the extraction of atomically resolved indium and nitrogen composition maps by evaluating strain and contrast in transmission electron microscopic two-beam images simultaneously. As the fringe contrast is compared with Bloch wave simulations, which in turn require accurate structure factors, we exemplify the influence of SAD and bonding on composition profiles regarding an $In_{0.08}Ga_{0.92}N_{0.03}As_{0.97}$ quantum well structure. In this respect, imaging conditions may be chosen for which SAD are of minor influence for conventional transmission electron microscopy, whereas relative errors larger than 25% can arise for the compositions if bonding is neglected.

DOI: 10.1103/PhysRevB.81.075315 PACS number(s): 68.37.Lp, 68.37.Og, 31.15.A−

I. INTRODUCTION

The investigation of semiconductor nanostructures using transmission electron microscopy (TEM) is an important feedback for the improvement and understanding of epitaxial and degradation processes of optoelectronic devices such as laser diodes and solar cells. During the last decades, several experimental techniques in the field of TEM established to measure local chemical composition. Any approach, for example the quantitative interpretation of annular dark field scanning TEM (STEM) images,[1] high-resolution lattice fringe[2] or dark field[3,4] images, relies on comparison with simulated reference data. As a consequence, calculation and modeling of accurate theoretical electron scattering factors which take into account chemical bonding[5] and static atomic displacements (SADs) due to different atomic radii[6] remains an important topic.

The concept to describe the scattering power of a crystal by means of the structure factor for the Bravais cell has proven to yield reliable results for the calculation of Bragg intensities using, e.g., the Bloch wave formalism. Thermal disorder is usually accounted for by correcting atomic scattering amplitudes (ASAs) with Debye-Waller factors and absorptive potentials derived from them. It has recently been shown that bonding effects can be incorporated in the 200 structure factor of ternary $In_xGa_{1-x}As$ via modified atomic scattering amplitudes (MASAs).[5,7] However, the MASA are derived from ideal binary crystals, so that SAD are not included yet but considered in terms of further correction factors, which are usually obtained from valence force field (VFF) methods applied to large cells.[5,8]

As doping of $In_xGa_{1-x}As$ with nitrogen on the arsenic sublattice induces strong local strain fields, the neglect of SAD in $In_xGa_{1-x}N_yAs_{1-y}$ alloys can lead to significantly erroneous scattering factors. We therefore first report on theoretical concepts for the computation of structure factors for $In_xGa_{1-x}N_yAs_{1-y}$ in Sec. II, where the reliability of the VFF relaxation is checked by means of residual forces obtained from density-functional theory (DFT) applied to large supercells with 216 atoms. Additionally, corresponding DFT scattering factors are compared with atomistic models such as MASA and ASA with and without the inclusion of SAD.

In Sec. III, we report on the extension of the composition evaluation by lattice fringe analysis (CELFA[2]) method to quaternary systems. In particular, we measure both x and y with atomic resolution from strain and contrast in a single TEM lattice fringe image of a solar cell diode acquired under a two-beam condition. An analysis of the application of different atomistic models together with systematic errors arising from unknown specimen thickness and concentration gradients will be given. This report closes with the discussion of the experimental results in the framework of bonding

TABLE I. Parameters used for the VFF and DFT calculations. DFT Lattice parameters have been calculated by Schowalter *et al.*[10] Elastic constants are taken from a review by Vurgaftman *et al.*[11]

Property	InN	InAs	GaN	GaAs
a_{EXP}[nm]	0.5004	0.6058	0.4519	0.5653
a_{DFT}[nm]	0.4945	0.6038	0.4460	0.5612
C_{11}[GPa]	223	83	293	122
C_{12}[GPa]	115	45	159	57
r_0[nm]	0.2167	0.2623	0.1957	0.2448

effects and SAD and conclusions as to the accuracy of composition evaluation techniques will be drawn.

II. VALENCE FORCE FIELD AND FIRST-PRINCIPLES CALCULATIONS

An accurate way to treat a quaternary structure including SAD is to place indium and nitrogen atoms at random positions of the respective sublattice in an ideal crystal and to use this structure as an initial guess for a relaxation based on forces derived from first principles. In order to not only reduce the computational effort drastically, but also to compare VFF calculations with *ab initio* calculations as to the residual forces, we sourced out the structure relaxation using empirical potentials and then performed only one DFT calculation using the WIEN2K[9] code.

A. Minimization of strain energy

In a $3\times3\times3$ GaAs supercell with 216 atoms, we replaced 0, 3, 6, 9, or 12 Ga atoms randomly by In and 0, 1, 2, 3, or 4 As atoms by N. This corresponds to a 5×5 grid of concentrations between 0 and 0.111 for In and between 0 and 0.037 for N, respectively. To derive a property $\alpha(x,y)$ for $In_xGa_{1-x}N_yAs_{1-y}$ from properties of binary crystals, interpolation according to

$$\alpha(x,y) = xy\alpha_{InN} + x(1-y)\alpha_{InAs} + \cdots,$$

$$y(1-x)\alpha_{GaN} + (1-x)(1-y)\alpha_{GaAs} \quad (1)$$

was performed, e.g., for the lattice parameters. Atom positions corresponding to the minimal strain energy of the supercell were found using the Keating[8] VFF model as described in Ref. 3. Elastic constants, lattice parameters and bond lengths $r_0 = a_{EXP}\sqrt{3}/4$ are listed in Table I.

B. Density-functional theory

For each of the 25 structures, DFT calculations have been performed in local density approximation with a force convergence of 0.01 mRy/bohr and 14 k points. The product of cutoff energy and the minimum muffin-tin radius (RK_{max}) was 6.0. A self-consistent solution was found after 20–30 cycles, depending on the respective supercell. Consistency with calculations using 28 k points and $RK_{max}=7.0$ was checked. Equilibrium lattice parameters for the binary crystals have also been found by DFT (Ref. 10) and are listed in Table I.

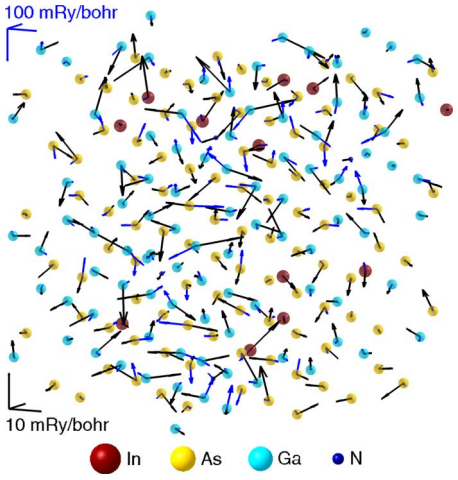

FIG. 1. (Color online) Residual forces resulting from DFT for a supercell containing 12 In and 4 N atoms before (blue) and after (black) VFF optimization. The trihedra top and bottom left refer to the scaling of the respective force vectors.

1. Residual forces

Resulting force vectors for each atom are depicted in Fig. 1 exemplarily for the supercell containing 12 In and 4 N atoms. We regard the discussion of this cell as the most representative because it contains the most dopant atoms. Blue and black vectors indicate the forces acting on each atom before and after the VFF relaxation, respectively. As the trihedra in Fig. 1 indicate, the VFF relaxation reduces the forces approximately one order of magnitude. Moreover, it can be seen that strong forces occur in the vicinity of substitutional In and N atoms for the unrelaxed supercell, whereas the magnitudes and directions of force vectors in the relaxed cell are distributed more or less statistically. In the picture of the VFF method, we must therefore interpret these forces of maximal 10 mRy/bohr as a systematical error of this approach for a relaxed supercell.

As the magnitude of these forces is still larger than typical residual forces after structure optimization using DFT only, we address the impact of this error on SAD in the following. This was done using a 64-atom $2\times2\times2$ supercell with 3 In atoms and 1 N atom. First, atom positions have been optimized by our VFF program, and second, this structure was further optimized using WIEN2K. In this way, we obtained difference vectors which point from the atom positions found by DFT to the respective position found by VFF and are thus, a direct measure of the error for the SAD computed with the VFF approach. Figure 2 depicts these difference vectors in black for each atom magnified by a factor of 50. It can be seen that discrepancies between VFF and DFT are statistically distributed and not concentrated on specific sites of, e.g., the dopant atoms. The blue vectors in Fig. 2 depict the SAD directly, magnified by a factor of 5. Here, the strong local lattice distortions induced by the nitrogen atom bottom right becomes obvious. As to the accuracy of the VFF method, we conclude that differences to DFT results, being

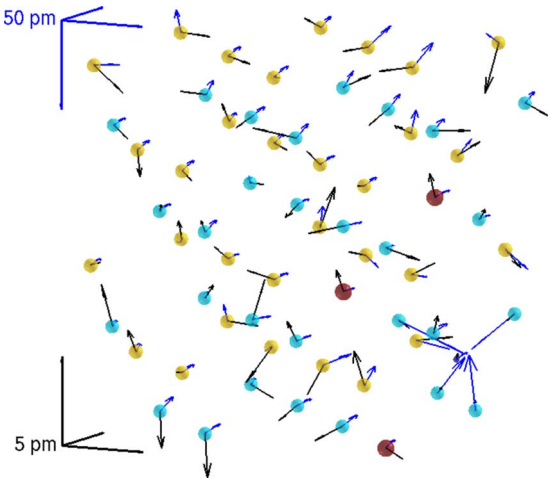

FIG. 2. (Color online) Static atomic displacements (blue, enlarged by a factor of 5) obtained by VFF and difference vectors (black, enlarged by a factor of 50) which point from the VFF atomic positions to those found by DFT. Because of the computational demanding DFT relaxation, we used a smaller $2\times2\times2$ supercell in this case containing 3 In atoms and 1 N atom. The nomenclature of the atoms is the same as in Fig. 1. See the blue or black trihedron top and bottom left for an absolute scaling of the SAD and difference vectors, respectively.

2.58 pm in the maximum, are more than an order of magnitude lower than the SAD themselves, which take values up to 37.96 pm. Therefore, the error falls in the range of thermal vibrational amplitudes, which are typically a few picometers in magnitude, so that atom positions deduced from VFF are physically plausible, even with residual forces found in Fig. 1.

2. Structure factors

Finally, x-ray structure factors have been calculated using the linearized-augmented plane wave routine LAPW3 and converted to electron structure factors using the Mott-Bethe formula.[5,12] These DFT structure factors for the relaxed supercells can be used to analyze the reliability of atomistic models as to the effects of bonding and SAD.

In terms of atomic scattering amplitudes f_j^κ, the structure factor takes the form,

$$V_{\vec{g}} = \frac{2\pi\hbar_P^2}{|e|m_e\Omega(\vec{a})}\sum_j^n f_j^\kappa[g(\vec{a})]e^{2\pi i\vec{g}(\vec{a})\vec{r}_j - B_j^\kappa/4g(\vec{a})^2}. \qquad (2)$$

This equation contains Planck's constant $h_P=2\pi\hbar_P$, mass m_e and charge e of an electron, the number of atoms n in the unit cell with volume $\Omega(\vec{a})$, Debye parameters B_j^κ, reciprocal lattice vectors $\vec{g}(\vec{a})$ and atom positions $\vec{r}_j$. The components of vector $\vec{a}$ equal the lattice constants to allow for the inclusion of strain. The main difference between Eq. (2) and the traditional definition of $V_{\vec{g}}$ is that bonding effects enter via MASA, which not only depend on atomic species j but also on the crystal κ where the respective atom is embedded in. For alloys, we first derive MASA f_j^κ from binary crystals listed in Table I using DFT as proposed by Rosenauer *et al.*[5] For example, two MASA for Ga are derived, one from a GaN crystal and the other from GaAs, representing the two types of bonds occurring for Ga in (InGa)(NAs). In order to calculate f_j^κ in a mixed (super)cell, we then average over the four MASA corresponding to the bond types and lengths defined by the four neighbor atoms. As lattice parameters and bond lengths of the alloy depend on chemical composition, MASA are calculated for a range of lattice parameters and enter Eq. (2) according to the lattice parameter of the respective alloy. Note that Eq. (2) also holds for conventional ASA in isolated atom approximation if the dependence on κ is omitted.

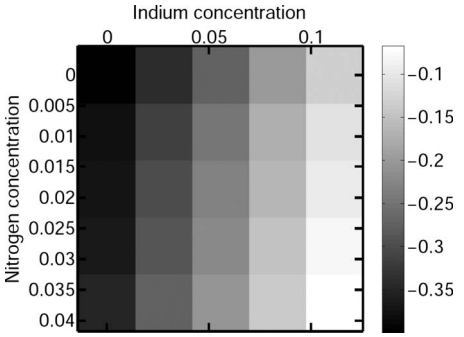

FIG. 3. V_{200} (real part) in volts as a function of In and N content obtained from first principles for the relaxed $3\times3\times3$ (InGa)(NAs) supercells. Concentrations correspond to 0, 1, 2, 3, 4 N and 0, 3, 6, 9, 12 In atoms, respectively.

We start with the analysis of the chemically sensitive 200 structure factor.[13] The result obtained from DFT for the relaxed supercell is depicted in Fig. 3 in dependence on the indium and nitrogen content. Even for the small concentration ranges considered here, Fig. 3 exhibits strong but smooth variation of $\mathrm{Re}(V_{200})$ with composition, as it is typical for chemically sensitive zinc blende systems. In the following, we assume that the data in Fig. 3 represent the most accurate scattering data for the 25 supercells considered, because no model assumptions concerning SAD and ASA entered the simulations. Therefore, we can use these structure factors as a reference to check the accuracy of atomistic models.

To this end, four analogous maps to Fig. 3 have been calculated using (a) modified and (b) isolated ASA with atom positions in the relaxed supercell, as well as (c) modified and (d) isolated ASA with atom positions in the unrelaxed supercell. To present the results in a compact manner, the structure factors obtained this way were subtracted from those in Fig. 3, yielding the differences depicted as histograms in Fig. 4. Thus, we would expect an absolute frequency of 25 at zero for an exact model.

From the view of atomistic models, Fig. 4 can be interpreted as follows: for first two data sets (a) and (b), V_{200} was calculated from Eq. (2) with correct atom positions r_j in a relaxed supercell, in combination with MASA (first row) and isolated ASA (second row). Obviously, the neglect of bonding effects can lead to large deviations of 0.054–0.123 V. In contrast, the bars of set (a) are concentrated relatively close around zero, where an 0.015 V too large structure factor is found in the worst case. However, the MASA concept together with SAD yields the most accurate and most precise

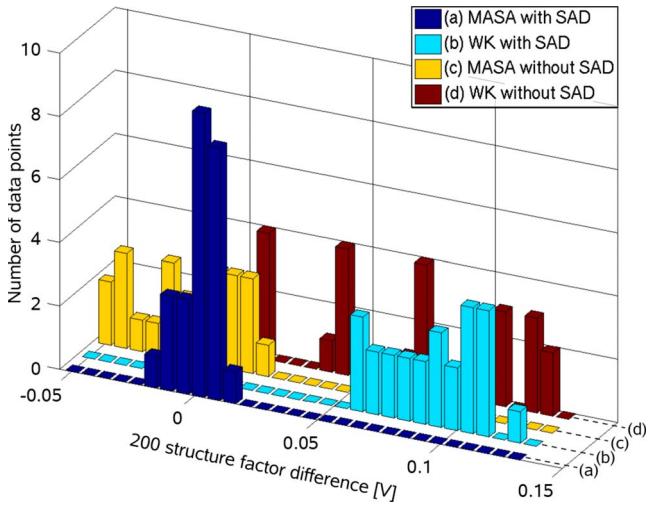

FIG. 4. (Color online) Histogram to show the reliability of different atomistic models (see legend) for the 200 structure factor. Differences between the 25 structure factors in Fig. 3 and those obtained from the respective model have been calculated and the absolute frequency is shown for 29 difference intervals. Data sets (a) and (c) contain bonding effects via MASA, (b) and (d) correspond to isolated atom scattering data due to Weickenmeier and Kohl (WK[14]). Furthermore, (a) and (b) contain SAD, (c) and (d) do not.

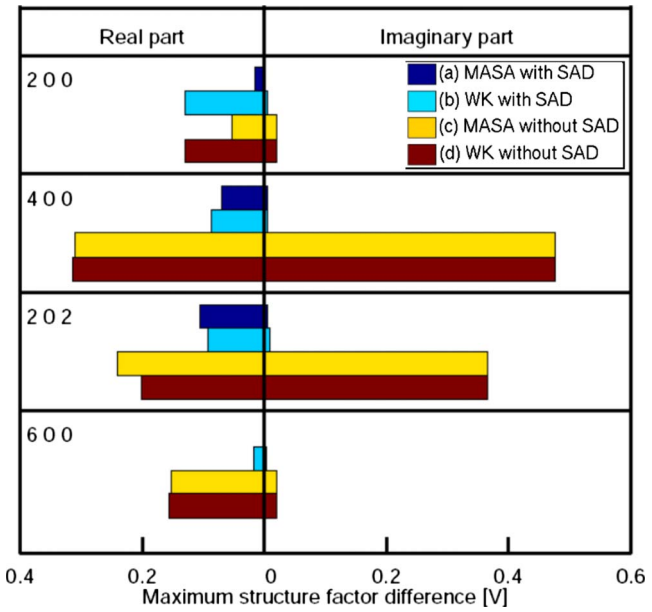

FIG. 5. (Color online) Diagram to show the largest difference between structure factors obtained from several atomistic models (see legend) and those calculated by DFT [see Fig. 3 for Re(V_{200})]. Real and imaginary parts are treated separately, and only moduli of differences are given. Data sets (a) and (c) contain bonding effects via MASA, (b) and (d) correspond to isolated atom scattering data due to Weickenmeier and Kohl (WK[14]). Furthermore, (a) and (b) contain SAD, (c) and (d) not.

200 structure factor for the structures considered here. Data sets (c) and (d) both exhibit a much lower precision than the respective counterparts (a) and (b). In the case of MASA without SAD, (c), a tail toward negative differences develops, which means that the structure factors obtained this way are principally too large.

We close our analysis of atomistic models for scattering factors with some comments on higher-order structure factors which are of importance, e.g., for the simulation of reference data for chemical compositional analysis or conventional TEM images in zone axis. For the 400, 202, and the chemically sensitive 600 structure factors, analogous maps to Fig. 3 have been calculated using the approximations (a)–(d) described above. To give an overview over the results, the largest deviation from the DFT structure factors analogous to Fig. 3 has been calculated for both the real and the imaginary parts and is plotted in Fig. 5, together with the V_{200} results. It can clearly be seen that the discrepancy between the MASA model (a) and (c) and isolated atom scattering factors (b) and (d) becomes negligible for higher order structure factors. This expresses the fact that low-order structure factors are most sensitive to electron redistributions due to bonding. Note that the 400 and 202 structure factors are more than an order of magnitude larger than V_{200}, which relativises the seemingly large error. For example, we find real parts of $V_{200}=-0.149$ V, $V_{400}=4.667$ V, $V_{202}=6.783$ V, and $V_{600}=-0.03$ V for $x=0.083$ and $y=0.028$, which is very close to the composition of the sample analyzed experimentally in Sec. III. However, the neglect of SAD can produce enormous errors as the bars corresponding to approaches (c) and (d) take large values of nearly half a volt. Depending on the structure factor, this corresponds to a relative error of 3%–40%.

We conclude that SAD must be considered in $In_xGa_{1-x}N_yAs_{1-y}$ systems in order to get reliable structure factor amplitudes and phases. The use of MASA is important mainly for the 200 structure factor and approaches isolated atom scattering data for higher spacial frequencies. This is because electron redistributions due to chemical bonding primarily affect the outermost orbitals of an atom, which corresponds to low-spatial frequencies in the Fourier spectrum. However, not only the dynamical interaction among diffracted beams but also the correct intensity of the 200 reflection require bonding effects to be considered for a quantitative comparison between experiment and simulation.

III. EXPERIMENTAL COMPOSITION QUANTIFICATION IN $In_xGa_{1-x}N_yAs_{1-y}$

A. Methodical summary

The composition of ternary zinc blende alloys such as (InGa)As has been extensively studied in the past either with respect to lattice strain or normalized 200 lattice fringe contrast.[2] Both quantities are usually measured from lattice fringes acquired by inserting an objective aperture around the beams $\vec{g}_1=000$ and $\vec{g}_2=200$. In quaternary systems, local strain and normalized 200 fringe amplitude must be measured simultaneously to allow for a unique composition determination. The image intensity at position $\vec{r}$ reads

$$I(\vec{r}) = A_1^2 + A_2^2 + 2A_1A_2T_{12}\cos(2\pi\vec{g}_2\vec{r} - \phi_{12} - \varphi_{12}), \quad (3)$$

where $A_n \exp(i\varphi_n)$ is the amplitude of diffracted beam $\vec{g}_n$, $\varphi_{12}=\varphi_1-\varphi_2$ is the phase difference between the two beams

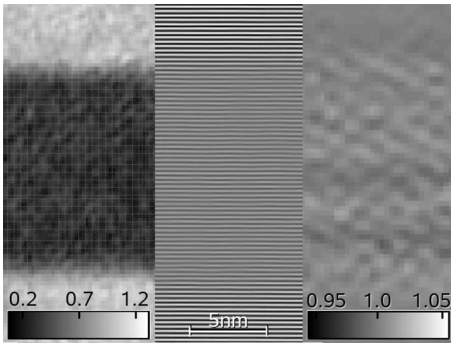

FIG. 6. Evaluation of contrast and strain in an experimental 200 lattice fringe image. The central part shows the recorded fringe image (part) which has been noise filtered for better visibility. The map on the left depicts the fringe amplitude normalized to GaAs as defined in Eq. (4). On the right, the local strain is shown, which was measured from local cosine fit in the fringe image.

and $T_{12}\exp(i\phi_{12})$ denotes the transmission cross coefficient. Note that most quantities in Eq. (3) do not only depend on composition, but also on thickness and specimen tilt in general, an aspect which we will discuss later. The measured quantity is the normalized fringe amplitude a_{200} defined by

$$a_{200}(x,y,t) = \frac{A_1(x,y,t)A_2(x,y,t)}{A_1(0,0,t)A_2(0,0,t)}, \tag{4}$$

meaning that the contrast is not measured absolutely but normalized to GaAs.

The central part of Fig. 6 depicts an experimental 200 lattice fringe image acquired with a specimen tilt corresponding to a Laue circle center of (1.5, 0, 20). The bright fringes top and bottom correspond to the GaAs buffer layers enclosing an (InGa)(NAs) quantum well grown by metal organic vapor phase epitaxy which exhibits a significantly lower contrast. By applying an aperture around the 200 reflection in the diffractogram and inverse Fourier transformation, we obtain the local distribution of the 200 fringe amplitude. In practice, regions with known composition, in this case the GaAs buffer layers, are used for a fifth-order polynomial fit of a surface serving as a reference where the measured signal is normalized to.

A map of a_{200} derived this way is shown on the left in Fig. 6. It can clearly be seen that the normalized amplitude in the quantum well region takes only about 30% of that in the GaAs substrate. In order to measure the strain depicted on the right in Fig. 6 with subpixel precision, we first determined the pixels with highest intensity on each fringe, second we refined these positions by local cosine fit according to Eq. (3), and third the local fringe distance was normalized to the average value measured in the GaAs buffer. The strain map exhibits a lattice-matched growth with slight strain fluctuations of less than 1%, which may arise from uncertainties in the strain measurement due to the low contrast in the quantum well area. By comparison of the local normalized amplitude and the local strain with corresponding reference data, atomic-scale concentration maps for indium and nitrogen can be derived.

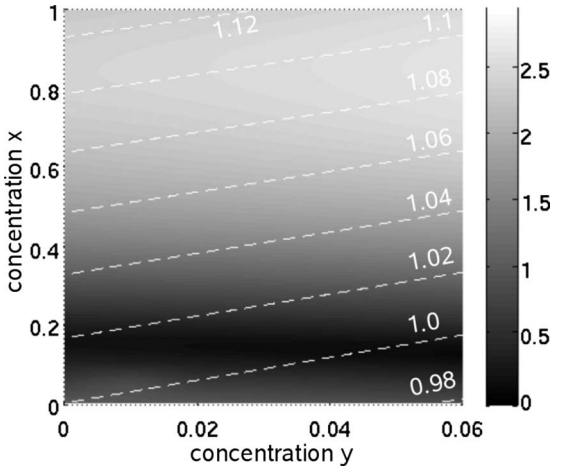

FIG. 7. Reference data for $a_{200}(x,y,50\text{ nm})$ (greyscale) and strain (dashed white contour lines). In the case shown here, atomic scattering factors contained bonding and SAD via MASA and SAD correction factors, respectively. Simulations have been carried out for a thickness range of 0–100 nm, of which the 50 nm simulation is shown. Both data sets correspond to a relaxation of $r=0.5$.

B. Simulation of reference data

The composition-dependent strain in growth direction was derived from elasticity theory corresponding to Hooke's law in combination with Eq. (1) using lattice parameters a_{EXP} and elastic constants C_{11} and C_{12} for the binary compounds given in Table I. It was assumed that an $In_xGa_{1-x}N_yAs_{1-y}$ quantum well is embedded dislocation free in GaAs and thinned along zone axis [010]. The relaxation along this axis was accounted for via a relaxation parameter $r\in[0\ldots1]$ being 0 for thin and 1 for thick samples.

According to Eq. (3), composition-dependent Bloch wave amplitudes have been calculated using these lattice parameters as input assuming each of the four atomistic models dealt with in Sec. II. A Laue circle center of (1.5, 0, 20) was used as for the experimental image in Fig. 6 and about 150 beams from two Laue zones have been included. Debye parameters were chosen according to Ref. 10 for 300 K. To include SAD, supercells with 10^6 atoms have been relaxed using the VFF program introduced in Sec. II and structure factors were derived from the relaxed cells.

Together with isostrain contours, Fig. 7 depicts a map of $a_{200}(x,y,50\text{ nm})$ according to Eq. (4) for indium contents $x\in[0\ldots1]$ and nitrogen contents $y\in[0\ldots0.06]$. As amplitude and strain contours incline an angle of about 20 degrees, an amplitude-strain pair can in principle be assigned a concentration pair (x,y). However, the null of the 200 structure factor defines a valley depicted in dark gray, so that two solutions exist below $x\approx0.35$. Nevertheless, it is in general no problem to distinguish between both because φ_{12} suffers a phase jump of π here which becomes obvious in the fringe image. Note that, although the 200 structure factor vanishes, the normalized amplitude still takes finite values of 10%–15%.

C. Composition maps and profiles

The distribution of indium and nitrogen derived from reference data including bonding via MASA and SAD via VFF

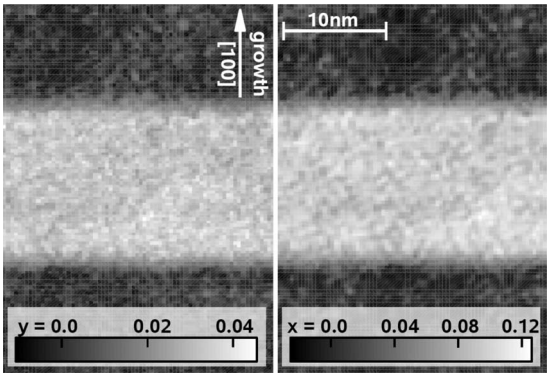

FIG. 8. Local distributions of indium and nitrogen in a quantum well region derived from reference amplitudes which include MASA and SAD according to Fig. 7.

is shown in Fig. 8. Both concentration maps exhibit a 15 nm wide quantum well with nearly uniform composition inside the well and gradual change at its edges. As to the state of relaxation in beam direction, it should be mentioned that it has no influence on the result for this structure since it was grown lattice matched to GaAs as depicted in Fig. 6.

The impact of bonding and SAD on composition evaluation is presented in the form of composition profiles shown in Figs. 9 and 10. Error bars represent the standard deviation for the lateral average in Fig. 8 and take values of 1% and 0.7% for indium and nitrogen, respectively. For both elements, we can divide the composition profiles into two pairs of curves of which one contains bonding (solid lines) and the other not (dashed lines). In both figures, the effect of MASA results in a decrease in the mean concentration being 0.03 for x and 0.01 for y. In contrast, SAD affect the profiles by a shift to larger concentrations as the black graphs show. However, this shift is very small as it lies within the error bars, indicating that imaging conditions are rather robust against the effect of SAD. Furthermore, a slight correlation of the indium and nitrogen profiles can be observed, which can be attributed to small fluctuations of the experimentally measured fringe amplitude according to Eq. (4). As Fig. 7 exhibits, this leads to little vertical shifts of the amplitude contours, either in or decreasing both x and y. Since this

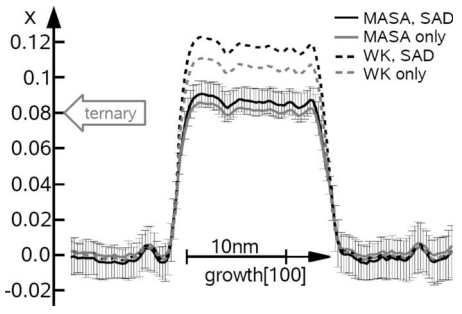

FIG. 9. Indium composition profiles calculated from maps analogous to the right composition map in Fig. 8 by averaging horizontally. The four curves differ in the reference data sets used, which are explained in the legend. The result for the mean indium concentration in a ternary (InGa)As well grown on the same sample during the same session is indicated by the gray arrow.

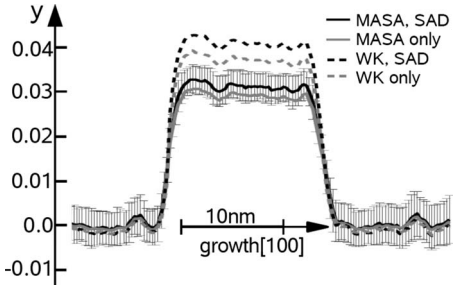

FIG. 10. Nitrogen composition profiles calculated from maps analogous to the left composition map in Fig. 8 by averaging horizontally. The four curves differ in the reference data sets used, which are explained in the legend.

correlation is well inside the error bars, it must rather be assigned to experimental errors than to a physical connection between the distribution of indium and nitrogen.

The most interesting aspect is to figure out which of the models applied in Figs. 9 and 10 is the most reliable one. For this purpose, an (InGa)As quantum well has been grown immediately after the quaternary well studied above to assure that growth conditions are comparable as far as possible, so that the same amount of indium should be observed. For two reasons, the results for the ternary system are more unique. Methodologically, the CELFA[2] method has frequently been applied to ternary structures and yielded reliable accuracy. Theoretically, it has been shown that the MASA approach is in best agreement with experiment here and that SAD have only minor influence on composition evaluation.[5] The gray arrow in Fig. 9 marks the result of $x=0.08\pm0.0075$ for the mean concentration obtained for the ternary alloy. We therefore conclude that only the MASA model is in agreement with the ternary result.

IV. DISCUSSION

A. Modeling of scattering properties

Section II was intended to give a detailed theoretical analysis of SAD and bonding effects on structure factors. Besides this, we have shown that atom positions obtained from VFF agree with DFT results within an accuracy in the range of thermal disorder even for relatively complex structures containing 12 Indium and 4 Nitrogen atoms. This is an important result regarding the simulation of STEM darkfield images, which are highly sensitive not only to thermal but also to static disorder.[1]

Concerning the modeling of structure factors via atomistic models, we add some further comments to the analysis in Sec. II B 2 First, the MASA model describes bonding effects on low order structure factors best in terms of the difference to full DFT calculations. Of course it would in principle be possible to use accurate DFT structure factors obtained from relaxed supercells in general, but note that the distribution of foreign substitutional indium and nitrogen atoms is of statistical nature which cannot (yet) be managed by DFT due to the strongly limited supercell size. Furthermore, the MASA approach allows for the inclusion of Debye–Waller factors as

conventionally defined. Second, Fig. 5 shows that SAD can severely affect structure factor phases for the 202 and 600 structure factor, which are real when neglecting SAD. This has already been pointed out by Glas,[6] and Fig. 5 exhibits that both isolated atom scattering amplitudes and MASA combined with SAD represent this effect with nearly the same accuracy. However, best agreement between full DFT calculations and atomistic approaches has already been reported in Refs. 3 and 5 for ternary materials if muffin-tin results from DFT are combined with SAD calculated by VFF.

Furthermore, our study shows that the consideration of SAD may result in larger moduli of the 200 structure factors whereas it acts as a damping factor regarding higher order structure factors. From Eq. (2) we see that the exponential terms may affect different atomic species differently, depending on the respective SAD. As the 200 structure factor is very small and essentially given by the difference between group III and group V ASA, this may result in a larger structure factor, explaining the fact that the consideration of SAD leads to higher concentrations in Figs. 9 and 10.

B. Methodical aspects

Since our method requires only the recording of a single two-beam image the experimental effort is very low on the one hand but still allows for atomically resolved concentration maps on the other. This is very important for an accurate study of diffusion and segregation processes in dependence on, e.g., annealing conditions on, which extensive studies have already been published in, e.g., Refs. 15 and 16. However, in comparison to the method proposed by Grillo *et al.*,[4] the method presented here overcomes the problem of correlating two images that contain chemically sensitive and strain information separately, and which were taken under very different specimen tilts in order to allow for a kinematic treatment of the 200 dark field amplitude. Nevertheless, our method requires the significant presence of 200 fringes, which is not given for all compositions as Fig. 7 shows. However, the dynamical simulation of (normalized) image contrast is essential since the 200 reflection vanishes for no concentration pair (x,y) whereas the 200 structure factor does.

As two beam imaging is based on the interference of scattered beams, we briefly address systematical errors arising from unknown specimen thickness, which may affect the normalized amplitude $a_{200}(x,y,t)$ in Eq. (4) and composition gradients, which can distort the strain maps according to φ_{12} in Eq. (3). In this respect it turned out that errors are dominated by the dependence on x, so that we present the analysis for a constant nitrogen content of 0.03, as it is typical for the experiment dealt with here.

According to Eq. (4), the elimination of the thickness dependence of $a_{200}(x,y,t)$ is desirable, if the specimen thickness is not measured separately. The black curve in Fig. 11 depicts the standard deviation $\sigma_t(x,0.03,t)$ of all amplitudes a_{200} corresponding to the same composition but different thicknesses in the range $t \in [10 \ldots 100\ \text{nm}]$. Up to $x \approx 0.5$, we indeed find that $\sigma_t < 0.05$. In the worst case, errors of

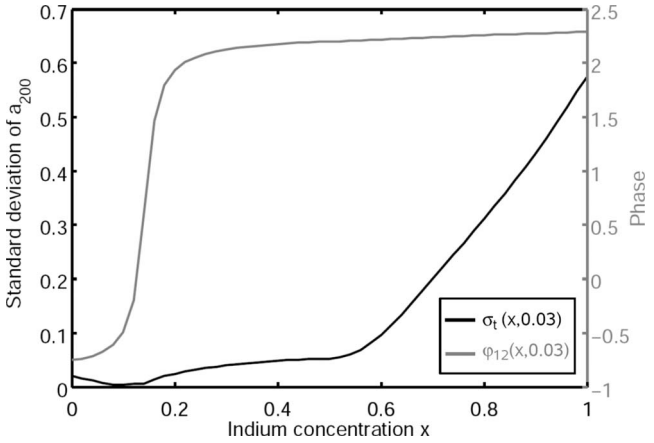

FIG. 11. Graphs to estimate systematical errors due to inaccurately known specimen thickness (black) and chemical shifts by concentration gradients (gray). Calculations were performed using the MASA model and SAD. The black curve depicts the standard deviation σ_t of a_{200} according to Eq. (4) calculated from a thickness range $t \in [10 \ldots 100\ \text{nm}]$. The phase φ_{12} occurring in Eq. (4) can cause invalid strain measurements if strongly depending on composition. As the gray curve exhibits, this is the case mainly near the phase jump region at $x \approx 0.15$. Only the result for $y=0.03$ is shown because the behavior of σ_t and φ_{12} is dominated by the dependence on x.

$\Delta x=0.01$ and $\Delta y=0.003$ can result then, which we found by comparison with Fig. 7. However, for larger concentrations x, either the thickness should be measured or the imaging conditions ought to be modified with respect to specimen tilt.

Since the positions of lattice fringes are not only determined by the lattice constant but also by the phase difference φ_{12} as expressed in Eq. (4), the gray graph was added to Fig. 11. It exhibits a widely flat behavior except for the phase jump region near $x \approx 0.15$. Since φ_{12} can only cause erroneous fringe positions in case of concentration gradients, we can trust the mean result of $\bar{x} \approx 0.08$ for the inner well region according to Fig. 8. From Figs. 9 and 10 we conclude that this is reached within about 10 monolayers, resulting in an average gradient of 0.008 per monolayer. Then, the gray curve in Fig. 11 exhibits a chemical phase shift of 0.025 near $x \approx 0.08$, resulting in an error $\Delta y=0.01$ for the respective fringe and even less for Δx. It may be due to this fact that all composition profiles in Figs. 9 and 10 show a slight enrichment of indium or nitrogen at the very edge of the well.

C. Composition profiles

As expected from the theoretical studies in Sec. II, Figs. 9 and 10 exhibit partly large differences in the resulting compositions, depending on the scattering data used. From the experimental point of view, the results for an equivalent ternary structure confirm an average indium content of $\bar{x}=0.08$, which, together with the fact that the well was grown lattice matched, means that the average nitrogen content is $\bar{y}=0.03$. This is in best agreement with bandgap and x-ray diffraction measurements by Volz *et al.*[17] For a sample grown under the same conditions a gap of 1 eV and a lattice-matched structure was found, which can uniquely be as-

signed to $In_{0.08}Ga_{0.92}N_{0.03}As_{0.97}$. Thus the MASA curves in Figs. 9 and 10 are the most plausible ones.

Concerning the effect of SAD on composition evaluation, Figs. 9 and 10 show that both MASA with and without SAD agree with each other within the experimental errors. For the indium profile, the solid gray curve is closest to the expected concentration whereas it is the solid black curve in the case of nitrogen. We, therefore, conclude that SAD have very little effect on composition evaluation for the experimental conditions and concentrations dealt with here. A Laue circle center of (1.5, 0, 20) corresponds to a systematic row condition where only a few beams are involved. Thus, the change in structure factor moduli and phases for higher order structure factors addressed in Sec. II B 2 has little influence on the 200 reflection due to a reduction of dynamical effects. However, large differences are observed for simulations in zone axis where the thickness dependence of beam amplitudes is altered significantly.

V. CONCLUSIONS

To include bonding effects in quaternary alloys in the simulation of electron scattering, structure factors may be derived from the respective binary constituents using DFT and the definition of MASA.[5] This not only allows for a high computational efficiency but can also be used to derive structure factors for a crystal of arbitrary composition. The atomistic MASA approach still holds if SAD are involved and a combination of both currently yields the most accurate Bragg intensities obtained, e.g., from Bloch wave simulations. In contrast to the isolated atom approach, MASA depend on the nearest-neighbor configuration of each atom in a supercell. They, therefore, principally allow for the treatment of correlated distributions of indium and nitrogen, as discussed in the frame of annealing procedures in Ref. 17.

As to the effect of SAD, we have shown that VFF and DFT calculations are in good agreement for a variety of quaternary structures with low concentrations. However, as the influence of SAD increases with scattering angle whereas bonding obeys the opposite trend, the concentration profiles presented here are altered rather by the inclusion of bonding than by SAD, in agreement with Ref. 5. Relative errors larger than 25% may arise if only isolated atom scattering data and a perfect crystal is assumed. The verification of VFF methods for (InGa)(NAs) by comparison with DFT is furthermore important for quantitative chemical mapping using dark field STEM, where the influence of SAD has already been stressed in Ref. 1 for ternary compounds.

The evaluation of strain and contrast in two beam lattice fringe images provides a simple method for the simultaneous measurement of indium and nitrogen composition in (InGa)(NAs) except for the concentrations near the phase jump of the 200 beam. Contrary to dark field images, this method allows atomically resolved chemical mapping analogous to the CELFA method, which is essential for the study of segregation and diffusion processes, which are known to modify optical properties of dilute nitrides crucially.[17]

ACKNOWLEDGMENTS

This work was supported by the Deutsche Forschungsgemeinschaft (DFG) under Contracts No. RO 2057/4 and No. SCHO 1196/3. K.M. also thanks the Physics International Postgraduate Programme (PIP) at Bremen University for sponsorship.

*mueller@ifp.uni-bremen.de

[1] V. Grillo, E. Carlino, and F. Glas, Phys. Rev. B **77**, 054103 (2008).
[2] A. Rosenauer, U. Fischer, D. Gerthsen, and A. Frster, Ultramicroscopy **72**, 121 (1998).
[3] O. Rubel, I. Németh, W. Stolz, and K. Volz, Phys. Rev. B **78**, 075207 (2008).
[4] V. Grillo, M. Albrecht, T. Remmele, H. P. Strunk, A. Y. Egorov, and H. Riechert, J. Appl. Phys. **90**, 3792 (2001).
[5] A. Rosenauer, M. Schowalter, F. Glas, and D. Lamoen, Phys. Rev. B **72**, 085326 (2005).
[6] F. Glas, Philos. Mag. **84**, 2055 (2004).
[7] K. Müller, M. Schowalter, J. Jansen, K. Tsuda, J. Titantah, D. Lamoen, and A. Rosenauer, Ultramicroscopy **109**, 802 (2009).
[8] P. N. Keating, Phys. Rev. **145**, 637 (1966).
[9] P. Blaha, K. Schwarz, G. K. H. Madsen, D. Kvasnicka, and J. Luitz, *Wien2k, an Augmented Plane* Wave+Local *Orbitals Program for Calculating Crystal Properties* (Technische Universität Wien, Austria, 2001).
[10] M. Schowalter, A. Rosenauer, J. T. Titantah, and D. Lamoen, Acta Crystallogr., Sect. A: Found. Crystallogr. **65**, 5 (2009).
[11] I. Vurgaftman, J. R. Meyer, and L. R. Ram-Mohan, J. Appl. Phys. **89**, 5815 (2001).
[12] J. C. H. Spence and J. M. Zuo, *Electron Microdiffraction* (Plenum Press, New York, 1992).
[13] For the $3\times3\times3$ supercells this corresponds to the 600 structure factor. However, we refer to the nomenclature for Bravais cells in this article.
[14] A. Weickenmeier and H. Kohl, Acta Crystallogr., Sect. A: Found. Crystallogr. **47**, 590 (1991).
[15] G. Patriarche, L. Largeau, J.-C. Harmand, and D. Gollub, Appl. Phys. Lett. **84**, 203 (2004).
[16] K. Volz, T. Torunski, O. Rubel, W. Stolz, P. Kruse, D. Gerthsen, M. Schowalter, and A. Rosenauer, J. Appl. Phys. **102**, 083504 (2007).
[17] K. Volz, W. Stolz, J. Teubert, P. J. Klar, W. Heimbrodt, F. Dimroth, C. Baur, and A. W. Bett, *Dilute III/V Nitride Semiconductors and Material Systems* (Springer, Berlin, Heidelberg, 2008), pp. 369–404.